

Oxygen Vacancy-Enhanced Ultrathin $\text{Bi}_2\text{O}_3\text{-Bi}_2\text{WO}_6$ Nanosheets' Photocatalytic Performances under Visible Light Irradiation

Jinwu Bai,* Xiaolei Ren,* Xue Chen, Peng Lu, and Min Fu



Cite This: *Langmuir* 2021, 37, 5049–5058



Read Online

ACCESS |



Metrics & More

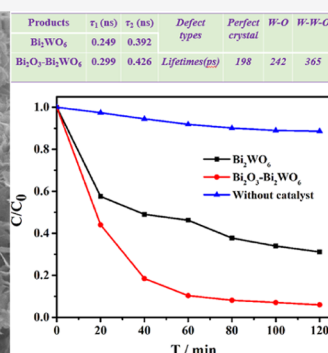
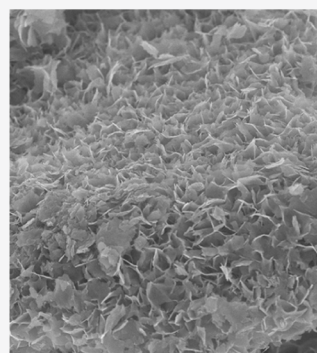


Article Recommendations



Supporting Information

ABSTRACT: The oxygen vacancy caused by ultrathin structures would be introduced into the semiconductor photocatalyst to boost its photocatalytic activity. Herein, ultrathin $\text{Bi}_2\text{O}_3\text{-Bi}_2\text{WO}_6$ nanosheet composites have been successfully synthesized via a facile hydrothermal method. Compared to pure Bi_2WO_6 nanosheets, the $\text{Bi}_2\text{O}_3\text{-Bi}_2\text{WO}_6$ nanosheet composites possess abundant oxygen vacancies, which was confirmed by the positron annihilation spectra. The ultrathin $\text{Bi}_2\text{O}_3\text{-Bi}_2\text{WO}_6$ nanosheet composites exhibited remarkable photocatalytic degradation performance for oxytetracycline compared with that of pure Bi_2WO_6 nanosheets. The excellent photocatalytic activities of $\text{Bi}_2\text{O}_3\text{-Bi}_2\text{WO}_6$ composites could be attributed to the heterojunction structure and the oxygen vacancies caused by ultrathin structures.



INTRODUCTION

Since the graphene came out in 2004,¹ two-dimensional (2D) graphene nanosheets have attracted wide attention because they possess fascinating physical and chemical properties.^{2–5} Particularly, 2D inorganic graphene-like nanosheet materials such as MoS_2 ,⁶ Co_3O_4 ,⁷ ZnGa_2O_4 ,⁸ TiO_2 ,⁹ MnO_2 ,¹⁰ and so forth exhibited excellent properties similar to graphene and have been extensively applied in electrocatalytics,¹¹ supercapacitors,¹² Li-ion batteries,¹³ solar cells,¹⁴ photocatalytics,¹⁵ and so on. The ultrathin 2D nanosheet structure has drawn attention to its application in the field of photocatalysis owing to the ultrathin structure endowing the 2D nanosheets miniscule atomic-scale thicknesses, large active surface areas,^{16–18} and fully exposed reaction activity sites.^{6,19} More importantly, the exposed atoms on the surface of 2D ultrathin nanosheets would easily escape from a lattice to form vacancies. At present, the introduction of vacancies to the surface of semiconductors is a promising strategy to improve the photocatalytic efficiency of semiconductors owing to vacancies often manipulating the change about the electronic properties of semiconductors.²⁰ Further work has manifested that the increased density of oxygen vacancies (donor density) can boost the transportation of charge, which results in the enhancement of photocurrent response and photocatalytic activity.²¹ It is reported that the existence of vacancy defects remarkable enhances the solar-driven photocatalytic activity of ultrathin BiOCl nanosheets.¹⁷ The TiO_2 nanocrystals that possessed surface defects exhibited excellent photocatalytic activity because the surface defects would significantly boost their separation efficiency of photogenerated carriers.²²

As one of the simplest Aurivillius family members, Bi_2WO_6 aroused intense interest owing to the layered structure and the excellent intrinsic physical and chemical properties.^{23,24} In particular, Bi_2WO_6 possesses suitable band gaps (2.6–2.8 eV), the ability of visible light absorption, high stability, nontoxicity, and an environmentally friendly feature, which was generally considered a promising visible light photocatalyst and would be practically applied in the field of wastewater purification.^{25,26} Previous research studies have confirmed that the Bi_2WO_6 nanomaterial has high photocatalytic activity,^{24,27,28} but the drawbacks of the fast electron–hole recombination rate in the photocatalytic process restrict its practical application.^{29–31} To settle the bottleneck, many strategies have been implemented to improve the catalytic efficiency of Bi_2WO_6 , such as the changing of morphologies,³² the modification of Bi_2WO_6 ,^{33–35} the construction of a heterojunction structure,^{31,36} and so on. Among them, the fabrication of a p–n junction structure between the n-type Bi_2WO_6 semiconductor and p-type semiconductors would be an effective strategy to improve the photocatalytic activity of Bi_2WO_6 . The p–n junction structure is conducive to enhance the separation of carriers and interfacial charge transfer efficiency, which would

Received: March 1, 2021

Revised: April 2, 2021

Published: April 13, 2021



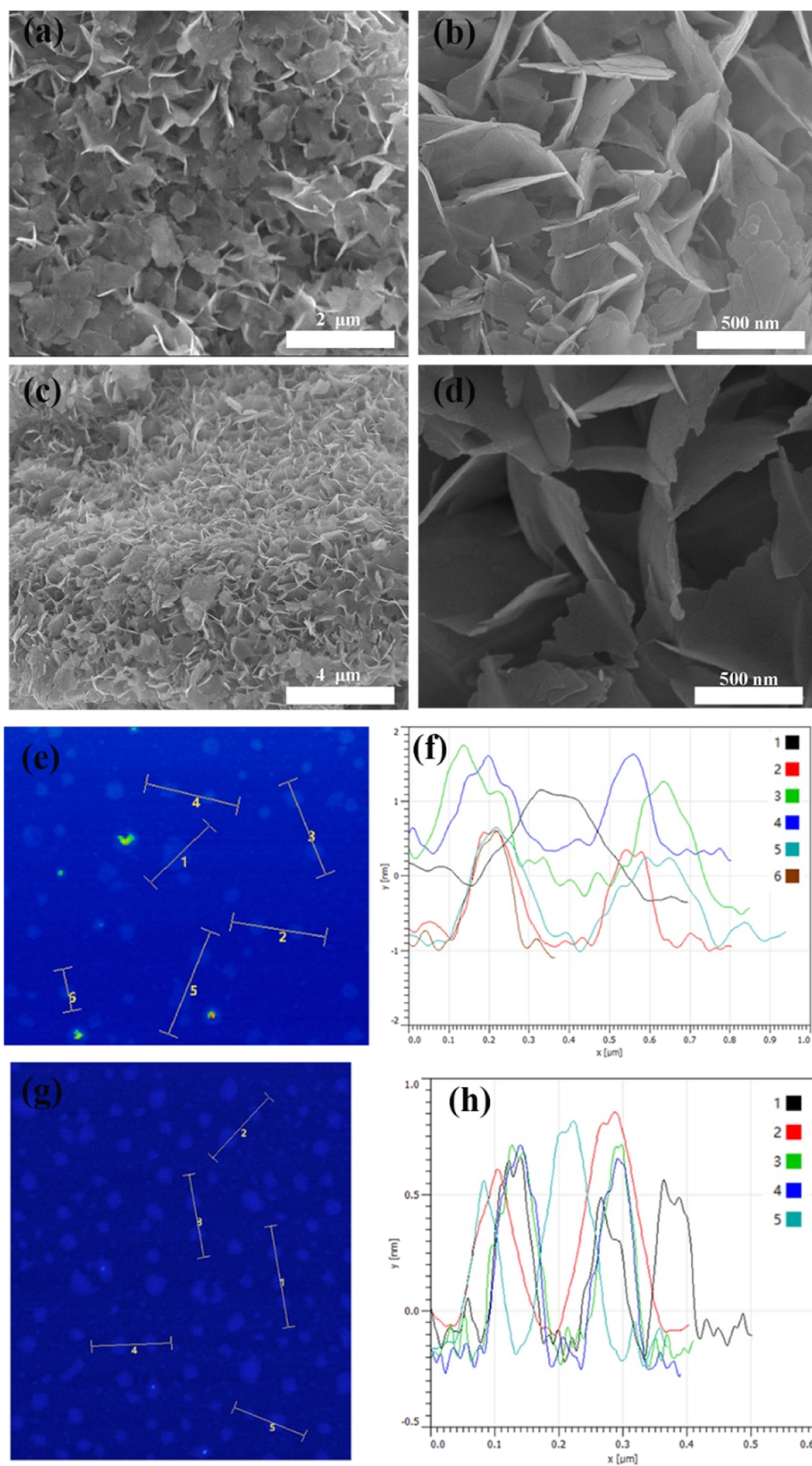


Figure 1. SEM images of the Bi_2WO_6 (a,b) and $\text{Bi}_2\text{O}_3\text{-Bi}_2\text{WO}_6$ composites (c,d); AFM images and height profiles of pure Bi_2WO_6 (e,f) and $\text{Bi}_2\text{O}_3\text{-Bi}_2\text{WO}_6$ samples (g,h).

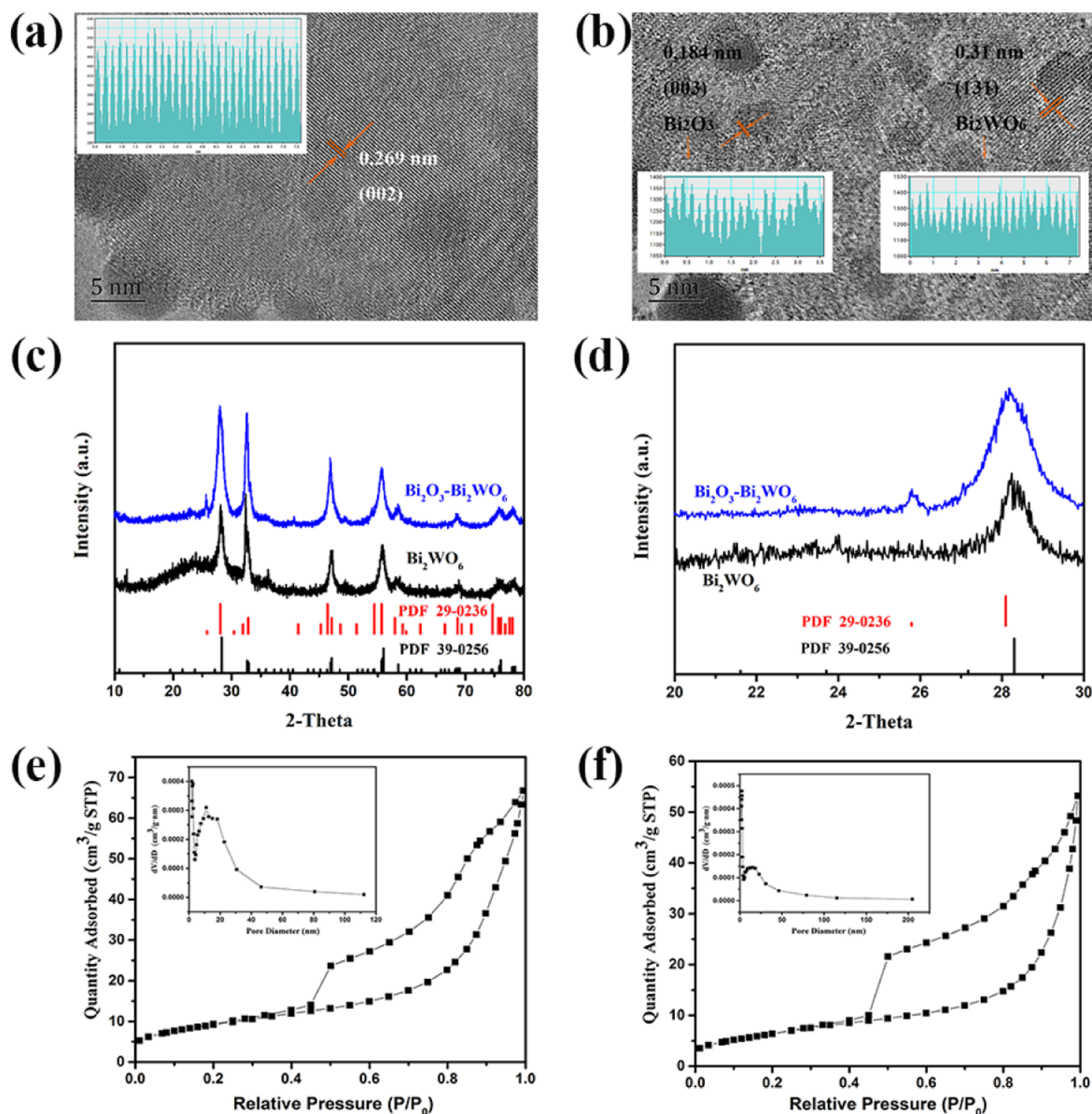


Figure 2. (a) HRTEM of Bi_2WO_6 ; (b) HRTEM of $\text{Bi}_2\text{O}_3\text{-Bi}_2\text{WO}_6$ composites; (c) XRD patterns of the Bi_2WO_6 and $\text{Bi}_2\text{O}_3\text{-Bi}_2\text{WO}_6$ composites; (d) magnified XRD patterns of the pure Bi_2WO_6 and $\text{Bi}_2\text{O}_3\text{-Bi}_2\text{WO}_6$ composites; nitrogen adsorption–desorption isotherms; and the corresponding pore size distribution plot (inset) of Bi_2WO_6 (e) and $\text{Bi}_2\text{O}_3\text{-Bi}_2\text{WO}_6$ composites (f).

be attributed to the existence of an internal electric field in the p–n junction.³⁷ As an intrinsic p-type semiconductor (~ 2.8 eV),³⁷ Bi_2O_3 can be a promising candidate semiconductor owing to that it could absorb some portion of visible light. The well-established $\text{Bi}_2\text{O}_3\text{-Bi}_2\text{WO}_6$ p–n heterojunction structure can be employed to inhibit the recombination of the photogenerated electrons and holes, which leads to large enhancement of the photocatalytic activity. In addition, because oxygen vacancies are known to exist in metal oxide materials,³⁸ the existence of WO_6 octahedra in Bi_2WO_6 or $\text{Bi}_2\text{O}_3\text{-Bi}_2\text{WO}_6$ would provide the feasibility of forming oxygen vacancies.^{39,40} Simultaneously, the ultrathin nanosheets would be beneficial to easily form oxygen vacancies in $\text{Bi}_2\text{O}_3\text{-Bi}_2\text{WO}_6$ nanosheets, which results in further promotion of its photocatalytic activity.

Hence, vacancy engineering would be introduced in the ultrathin $\text{Bi}_2\text{O}_3\text{-Bi}_2\text{WO}_6$ nanosheets to boost its photocatalytic activity. The positron annihilation technique and electron

paramagnetic resonance (EPR) spectra confirmed that the $\text{Bi}_2\text{O}_3\text{-Bi}_2\text{WO}_6$ composites possess more oxygen vacancies than Bi_2WO_6 nanosheets. During the photodegradation of oxytetracycline (OTC), the ultrathin $\text{Bi}_2\text{O}_3\text{-Bi}_2\text{WO}_6$ nanosheets exhibit much higher photocatalytic activities than Bi_2WO_6 nanosheets, which could be attributed to the synergistic effect of the heterojunction structure and the abundant oxygen vacancies aroused by the ultrathin structure.

EXPERIMENTAL SECTION

Synthesis of Ultrathin $\text{Bi}_2\text{O}_3\text{-Bi}_2\text{WO}_6$ Nanosheets. The chemical reagents used in experiments are of analytical grade. Typically, 0.97 g of $\text{Bi}(\text{NO}_3)_3 \cdot 5\text{H}_2\text{O}$ was dissolved in 10 mL of water acidified with 1 mL of concentrated nitric acid, and then, 0.05 g of sodium dodecyl sulfonate (SDS) was added with vigorous stirring for 10 min. Afterward, 20 mL of glacial acetic acid dissolved with 0.329 g of $\text{Na}_2\text{WO}_4 \cdot 5\text{H}_2\text{O}$ was added to the abovementioned mixture. After 30 min of agitation, the mixture was put in a 50 mL Teflon-lined stainless-steel autoclave, and the temperature was retained at 180 °C

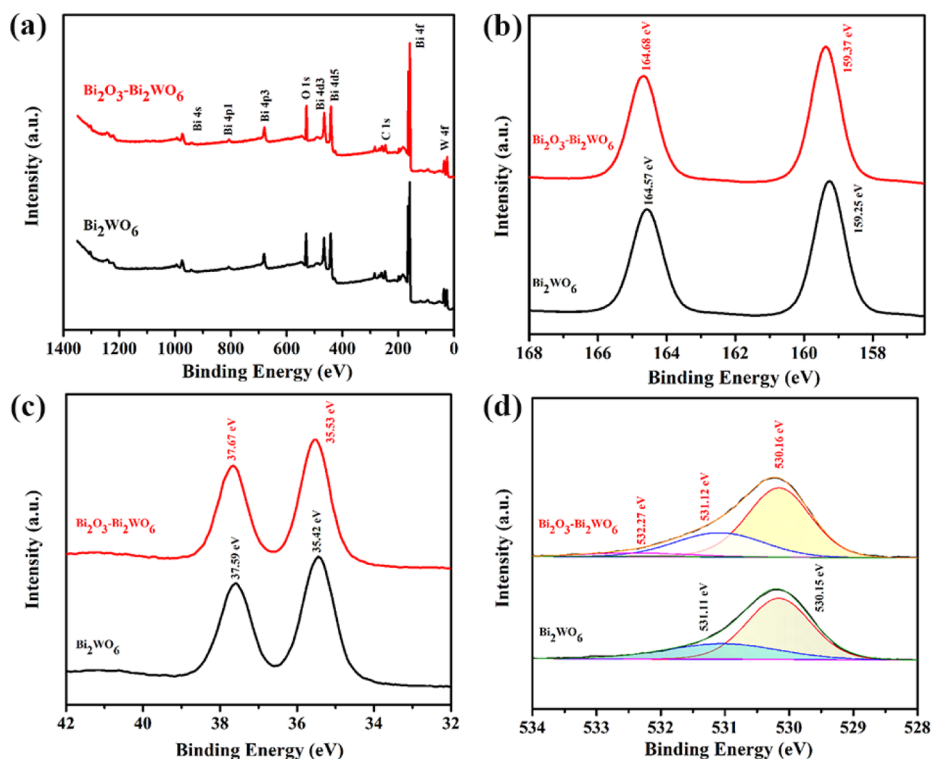


Figure 3. XPS spectra of as-prepared samples: (a) survey of the sample, (b) Bi 4f; (c) W 4f; and (d) O 1s.

for 24 h. Later, the products synthesized were collected and washed with distilled water and absolute ethanol. Finally, the final products were dried at 80 °C in air. The Bi_2WO_6 nanosheets were synthesized using the same method except for not adding the SDS. The pure Bi_2O_3 samples were obtained by calcining NaBiO_3 at 550 °C for 2 h.

Material Characterization. An X-ray diffractometer (XRD, Rigaku D/Max 2500) was used to analyze the X-ray diffraction patterns (XRD) of synthesized photocatalysts. The morphology and structure of the synthesized catalysts were observed by scanning electron microscopy (SEM) (Nova Nano SEM 230, FEI) and transmission electron microscopy (TEM) (Tecnai G2 F20, FEI). The apparatus of the Shimadzu UV-3600 recording spectrophotometer was used to characterize the absorption spectra of as-prepared products. X-ray photoelectron spectroscopy (ESCALAB 250Xi, Thermo Fisher Scientific) was utilized for the surface elemental analysis and measuring the valence band spectra of photocatalysts. The TriStar 3000 nitrogen adsorption apparatus was used to record the specific surface area of the prepared samples. EPR test was performed using the Bruker EMX nanoequipment at room temperature.

Photocatalytic Experiments. The photocatalytic activity measurement was conducted on the XPA-7 photochemical reactor, which was fabricated in Xujiang Electromechanical Plant, Nanjing, China. The photocatalytic activities of the photocatalysts were estimated by photodegradation of OTC under a 500 W Xe lamp. The procedure of photocatalysis is as follows: 0.050 g of the synthesized photocatalyst was added to 50 mL of 10 mg/L OTC aqueous solution and then stirred constantly. To achieve the adsorption–desorption equilibrium between the OTC and catalyst, the mixture was placed in a dark environment with stirring for 30 min. After irradiation, about 5 mL of the reaction solution at intervals of time was centrifuged and then filtered using a 0.22 μm membrane filter. Subsequently, the 752N UV–vis spectrophotometer was utilized to analyze the supernatant, and the wavelength chosen was 355 nm. Other photocatalytic tests were conducted using similar operation.

RESULTS AND DISCUSSION

The morphologies of as-prepared samples were characterized by low-magnification field-emission SEM and high-resolution TEM (HRTEM). The panoramic morphology (Figure 1a,b) displays that the pure Bi_2WO_6 samples consisted of nanosheets. The morphologies of as-prepared Bi_2O_3 – Bi_2WO_6 composites are shown in Figures 1c,d and S1a,b. The Bi_2O_3 – Bi_2WO_6 composites display flake-like morphologies, which are similar to those of pure Bi_2WO_6 samples. As is well known, the thickness of samples would be measured by atomic force microscopy (AFM). The AFM images and height profile of the Bi_2WO_6 and Bi_2O_3 – Bi_2WO_6 composites are shown in Figure 1e,f and g,h, respectively. The measured results indicate that Bi_2WO_6 and Bi_2O_3 – Bi_2WO_6 individual nanosheets are only a few atoms thick.

The TEM images (Figure S2a–c) further demonstrated the sheet-shaped architecture of pure Bi_2WO_6 samples, which agrees well with the microstructure of Bi_2WO_6 SEM images. In Figure S2d–f, the TEM images of Bi_2O_3 – Bi_2WO_6 displayed that the Bi_2O_3 – Bi_2WO_6 is composed of sheet-shaped nanosheets. The HRTEM image of the Bi_2WO_6 displayed that the interplanar spacing of adjacent fringes was about 0.269 nm, which is well matched with that of the (002) plane of Bi_2WO_6 (Figure 2a). In the HRTEM image of the Bi_2O_3 – Bi_2WO_6 (Figure 2b), the lattice fringe spacing was measured to be about 0.31 and 0.184 nm, consistent with the (131) plane of Bi_2WO_6 and the (003) plane of Bi_2O_3 , respectively. The abovementioned result indicated the formation of Bi_2O_3 – Bi_2WO_6 composites. The crystalline structure of the Bi_2WO_6 and Bi_2O_3 – Bi_2WO_6 composites was investigated by XRD. Figure 2c displays an X-ray diffraction (XRD) pattern of the as-prepared samples. All of the diffraction peaks of the pure Bi_2WO_6 nanosheets can be indexed to the Russellite phase of Bi_2WO_6 (JCPDS 39-0256). The XRD peaks of Bi_2O_3 – Bi_2WO_6

composites can be indexed to the monoclinic structure of Bi_2O_3 (JCPDS 29-0236) and orthorhombic Bi_2WO_6 (JCPDS 39-0256). The samples possess good sample crystallinity owing to the displayed sharp diffraction peaks of the samples. Figure S3 shows that the as-prepared Bi_2O_3 samples were pure materials. Moreover, no impurity peaks were detected. The magnified XRD patterns of the products in the range of 2θ (20.0–30.0) are shown in Figure 2d. The peak at 25.64 was well assigned to the Bi_2O_3 (JCPDS 29-0236), suggesting that the Bi_2WO_6 has the composition of Bi_2O_3 . The nitrogen adsorption–desorption isotherm of Bi_2WO_6 (Figure 2e) and Bi_2O_3 – Bi_2WO_6 composites (Figure 2f) can be assigned as type IV, belonging to the mesoporous materials. The pore size distribution data of pure Bi_2WO_6 and Bi_2O_3 – Bi_2WO_6 composites obtained from the isotherms (as shown in the insets of Figure 2e,f) illustrate a large number of pores of less than 12.5 and 15.1 nm, respectively. In the pore size distribution image of pure Bi_2WO_6 and Bi_2O_3 – Bi_2WO_6 , the smaller pores with a sharp peak at about 3.9 and 2.4 nm could have been originated from the process of crystal growth.⁴¹ The BET surface area of the Bi_2O_3 – Bi_2WO_6 composites is 22.22 $\text{m}^2 \text{g}^{-1}$, which is slightly lower than that of the pure Bi_2WO_6 (BET specific surface area was about 32.56 $\text{m}^2 \text{g}^{-1}$).

The X-ray photoelectron spectroscopy (XPS) spectra were characterized to reveal the surface elemental compositions, chemical state, and existence of O-vacancy spectra in Bi_2WO_6 and Bi_2O_3 – Bi_2WO_6 composites. Figure 3a shows that the survey XPS spectrum of Bi_2WO_6 and Bi_2O_3 – Bi_2WO_6 composites included Bi, W, O, and C elements. The high-resolution Bi 4f spectrum of Bi_2WO_6 (Figure 3b) can be divided into two different peaks at 164.57 and 159.25 eV, which can be ascribed to the level of Bi 4f_{7/2} and Bi 4f_{5/2}, respectively. The high-resolution W 4f spectrum of Bi_2WO_6 (Figure 3c) could be fitted into two peaks at 35.42 and 37.59 eV, which correspond to W 4f_{7/2} and W 4f_{5/2}, respectively. In comparison, the high-resolution Bi 4f and W 4f spectrum of Bi_2O_3 – Bi_2WO_6 (Figure 3b,c) shows about 0.1 eV shift to higher binding energy, which would be attributed to that the existence of oxygen vacancies changes the electron density.⁴² Furthermore, the high-resolution O 1s spectrum of Bi_2WO_6 (Figure 3d) would be separated into two peaks at 530.15 and 531.11 eV, which would be ascribed to the coordination of oxygen in Bi–O and W–O, respectively. The O 1s spectrum of Bi_2O_3 – Bi_2WO_6 can be deconvoluted to three peaks at 530.16, 531.12, and 532.27 eV, which would be attributed to the oxygen in Bi–O and W–O in Bi_2WO_6 and Bi–O in Bi_2O_3 , respectively.⁴⁰ As can be seen in Figure 3d, the contribution of Bi–O is decreased for Bi_2O_3 – Bi_2WO_6 , which implied the formation of oxygen vacancies.⁴³

The EPR spectra of Bi_2WO_6 and Bi_2O_3 – Bi_2WO_6 nanocomposites (as shown in Figure S4) further confirmed the existence of oxygen vacancies. To further validate the existence of oxygen vacancies, positron annihilation spectroscopy was utilized to study the defect of prepared materials, as shown in Tables 1 and S1. The longest component (τ_3) is caused by the

annihilation of ortho-positronium atoms formed in the large voids present in prepared materials.^{22,44} The shortest component (τ_1) would be ascribed to the free annihilation of positrons in defect-free crystals.⁴⁵ However, in disordered systems, monovacancies or shallow positron traps would decrease the average electron density and lead to an increase in the lifetime of τ_1 .^{22,46} It can be seen clearly that the τ_1 of the pure Bi_2WO_6 is higher than that of the perfect Bi_2WO_6 crystalline (198 ps, Table S1), which reveals the presence of small defects in the Bi_2WO_6 . According to the theoretically calculated positron lifetime values caused by different vacancies types (Table S1), the τ_1 of the pure Bi_2WO_6 (0.249 ns) would correspond to the type of W–O vacancies. As shown in Table 1, the Bi_2O_3 – Bi_2WO_6 composites show an obvious change of τ_1 , revealing a small amount of defects in the Bi_2O_3 . The τ_2 of pure Bi_2WO_6 is much larger than the τ_1 of pure Bi_2WO_6 , suggesting positrons trapped by larger sized oxygen vacancy clusters. The intermediate lifetime component τ_2 is generally attributed to the existence of larger size defects, for example, oxygen vacancy clusters in the materials.⁴⁷ Compared with small-size defects, the large defects possess lower average electron density, which would be in favor of decreasing the annihilation rate of the positron and increasing the positron lifetime.^{22,47} The τ_2 for the Bi_2O_3 – Bi_2WO_6 nanocomposites is much larger than that of pure Bi_2WO_6 , suggesting positrons trapped by larger sized oxygen vacancy clusters. In Bi_2O_3 – Bi_2WO_6 nanocomposites, the τ_1 and τ_2 show an obvious change, revealing that the composites possess abundant larger sized oxygen vacancy clusters located on the surface and subsurface.

The light absorption ability of the semiconductor related to its electronic structure features is identified as a pivotal factor in determining its photocatalytic activity.⁴⁸ Figure 4a presents that the Bi_2O_3 – Bi_2WO_6 composites show more intensive light absorption compared to pure Bi_2WO_6 . Figure S5a shows that the pure Bi_2O_3 has a strong light absorption ability. The optical absorption near the band edge of the crystalline semiconductor is expressed by the equation $ah\nu = A(h\nu - E_g)^{1/2}$, where α , ν , E_g , and A are the absorption coefficient, light frequency, band gap, and constant, respectively.²⁴ The band gap (E_g) of the Bi_2WO_6 is about 2.58 eV, which is based on the $(Ah\nu)^2 = f(h\nu)$ by the intercept of the tangent to the plot with abscissa (Figure 4b). Similarly, the E_g of Bi_2O_3 is about 2.63 eV (Figure S5b). In addition, the maximum energy edge of the VB of pure Bi_2WO_6 is at about 2.07 eV (Figure 4c). The conduction band (CB) of pure Bi_2WO_6 was evaluated by the following equation: $E_{\text{CB}} = E_{\text{VB}} - E_g$; the minimum CB edges of pure Bi_2WO_6 would occur at about –0.51 eV. Compared with that of pure Bi_2WO_6 , the VB maximum of Bi_2O_3 – Bi_2WO_6 nanocomposites upshifts from 2.07 to 1.75 eV, which would be attributed to the formation of the heterojunction,⁴⁹ as confirmed by XRD and XPS results. The constructed heterojunction would be beneficial to the separation of photogenerated electron–hole pairs, which was analyzed by the photoluminescence (PL) characterization. The PL spectra of pure Bi_2O_3 , Bi_2WO_6 , and Bi_2O_3 – Bi_2WO_6 at the excitation wavelength of 400 nm are shown in Figure 4d. Compared to Bi_2O_3 and Bi_2WO_6 , Bi_2O_3 – Bi_2WO_6 exhibited much lower emission peak intensity, indicating the higher separation rate of photogenerated carriers and then improvement in its photocatalytic activity.

The photocatalytic performance of Bi_2WO_6 and Bi_2O_3 – Bi_2WO_6 composites was investigated using photodegradation OTC in water under visible light irradiation. Figure 5a presents

Table 1. Positron Lifetime and Relative Intensities of the Pure Bi_2WO_6 and Bi_2O_3 – Bi_2WO_6

product	τ_1 (ns)	τ_2 (ns)	τ_3 (ns)	I_1 (%)	I_2 (%)	I_3 (%)
Bi_2WO_6	0.249	0.392	2.11	42.5	57.3	0.148
Bi_2O_3 – Bi_2WO_6	0.299	0.426	3.25	59.5	40.3	0.171

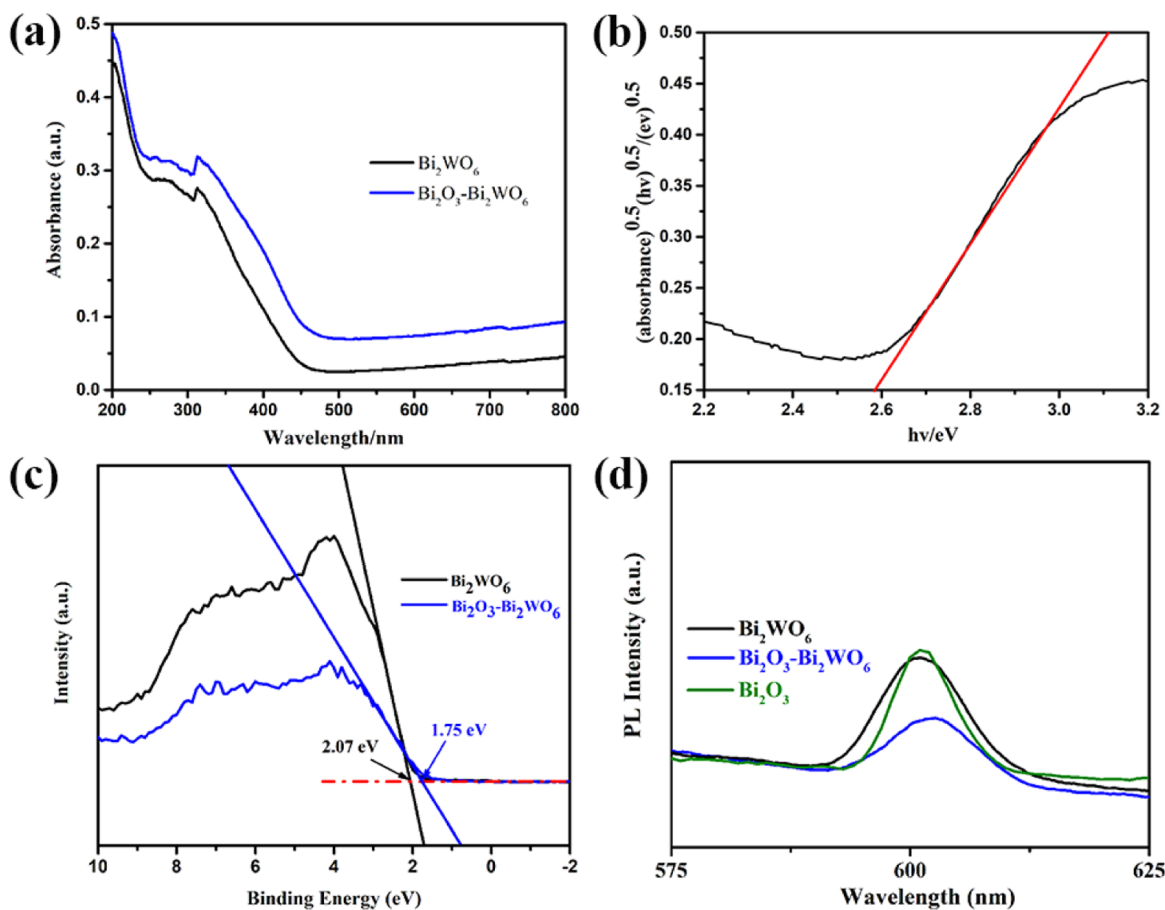


Figure 4. (a) UV–visible diffuse reflectance absorption spectra of Bi_2WO_6 and $\text{Bi}_2\text{O}_3\text{-Bi}_2\text{WO}_6$ composites; (b) $(Ah\nu)^{1/2}-h\nu$ curves of pure Bi_2WO_6 ; (c) valence band XPS spectra of pure Bi_2WO_6 and $\text{Bi}_2\text{O}_3\text{-Bi}_2\text{WO}_6$; and (d) PL spectra of pure Bi_2O_3 , Bi_2WO_6 , and $\text{Bi}_2\text{O}_3\text{-Bi}_2\text{WO}_6$ at the excitation wavelength of 400 nm.

the photocatalytic degradation curves of OTC with the time change, where C was the absorption of OTC at the wavelength of 355 nm after irradiation and C_0 was the absorption of OTC after the adsorption equilibrium on the photocatalyst before irradiation. As displayed in Figure 5a, the degradation efficiency of OTC without any catalyst under visible light was about 7%. In the process of photocatalytic degradation, the absorption ability of Bi_2WO_6 and $\text{Bi}_2\text{O}_3\text{-Bi}_2\text{WO}_6$ composites for OTC is an important element to its photocatalytic degradation rate. The removal efficiency of Bi_2WO_6 and $\text{Bi}_2\text{O}_3\text{-Bi}_2\text{WO}_6$ composites for OTC was increasing with time and reached 36 and 41% after 120 min, respectively. Figures S6 and 5a display that the photodegradation efficiency of Bi_2O_3 , Bi_2WO_6 , and $\text{Bi}_2\text{O}_3\text{-Bi}_2\text{WO}_6$ composites for OTC reached 86, 70, and 97% after 120 min of photocatalytic reaction, respectively. The results indicated that the $\text{Bi}_2\text{O}_3\text{-Bi}_2\text{WO}_6$ composites possess better photocatalytic activities than pure Bi_2WO_6 . Moreover, the mineralization rate of Bi_2WO_6 and $\text{Bi}_2\text{O}_3\text{-Bi}_2\text{WO}_6$ composites was evaluated by the total organic carbon removal efficiency, which helps us understand the photocatalytic degradation degree of OTC. The byproducts of OTC after photodegradation over the $\text{Bi}_2\text{O}_3\text{-Bi}_2\text{WO}_6$ composites were analyzed by ultra-performance liquid chromatography tandem mass spectrometry (UPLC–MS–MS) (Figure S7). Based on the result of UPLC–MS–MS and the relative literature,^{50–53} the proposed photodegradation pathway of OTC was deduced, as shown in Figure S8. It can be clearly seen that the OTC mineralization rate of $\text{Bi}_2\text{O}_3\text{-}$

Bi_2WO_6 composites is higher than that of Bi_2WO_6 (Figure S9). Furthermore, we also utilized the Bi_2WO_6 and $\text{Bi}_2\text{O}_3\text{-Bi}_2\text{WO}_6$ composites for photodegradation of the norfloxacin, which is difficult to biodegrade in conventional biological wastewater treatment plants. As shown in Figure S10, $\text{Bi}_2\text{O}_3\text{-Bi}_2\text{WO}_6$ composites exhibited much enhanced photocatalytic performance than pure Bi_2WO_6 . Meanwhile, the $\text{Bi}_2\text{O}_3\text{-Bi}_2\text{WO}_6$ composites have significantly photodegradation efficiencies to the tetracycline pollutants (Figure S11). These results implied that the introduction of Bi_2O_3 into the Bi_2WO_6 photocatalyst and possessing larger vacancy defects notably enhance the photoactivity performance of $\text{Bi}_2\text{O}_3\text{-Bi}_2\text{WO}_6$ composites. Furthermore, the stability and reusability of $\text{Bi}_2\text{O}_3\text{-Bi}_2\text{WO}_6$ composites were investigated by the recycling experiments. The photocatalytic activity of $\text{Bi}_2\text{O}_3\text{-Bi}_2\text{WO}_6$ composites reduced about 14% after three cycle experiments, but its photodegradation efficiency reached about 80% (Figure S12). The result demonstrated that the $\text{Bi}_2\text{O}_3\text{-Bi}_2\text{WO}_6$ composites would be a promising purification wastewater material in practical application.

As we all know, the photoinduced holes (h^+), superoxide radicals ($\text{O}_2^{\bullet-}$), and hydroxyl radicals ($\bullet\text{OH}$) are essential to photocatalytic oxidant(s) reaction, which is beneficial to the degradation of organic pollutants.²⁶ To study the photocatalytic degradation process of OTC by the Bi_2WO_6 and $\text{Bi}_2\text{O}_3\text{-Bi}_2\text{WO}_6$ composites, different scavengers were added to detect the major active species in the photodegradation process. Based on the previously reported literature, the

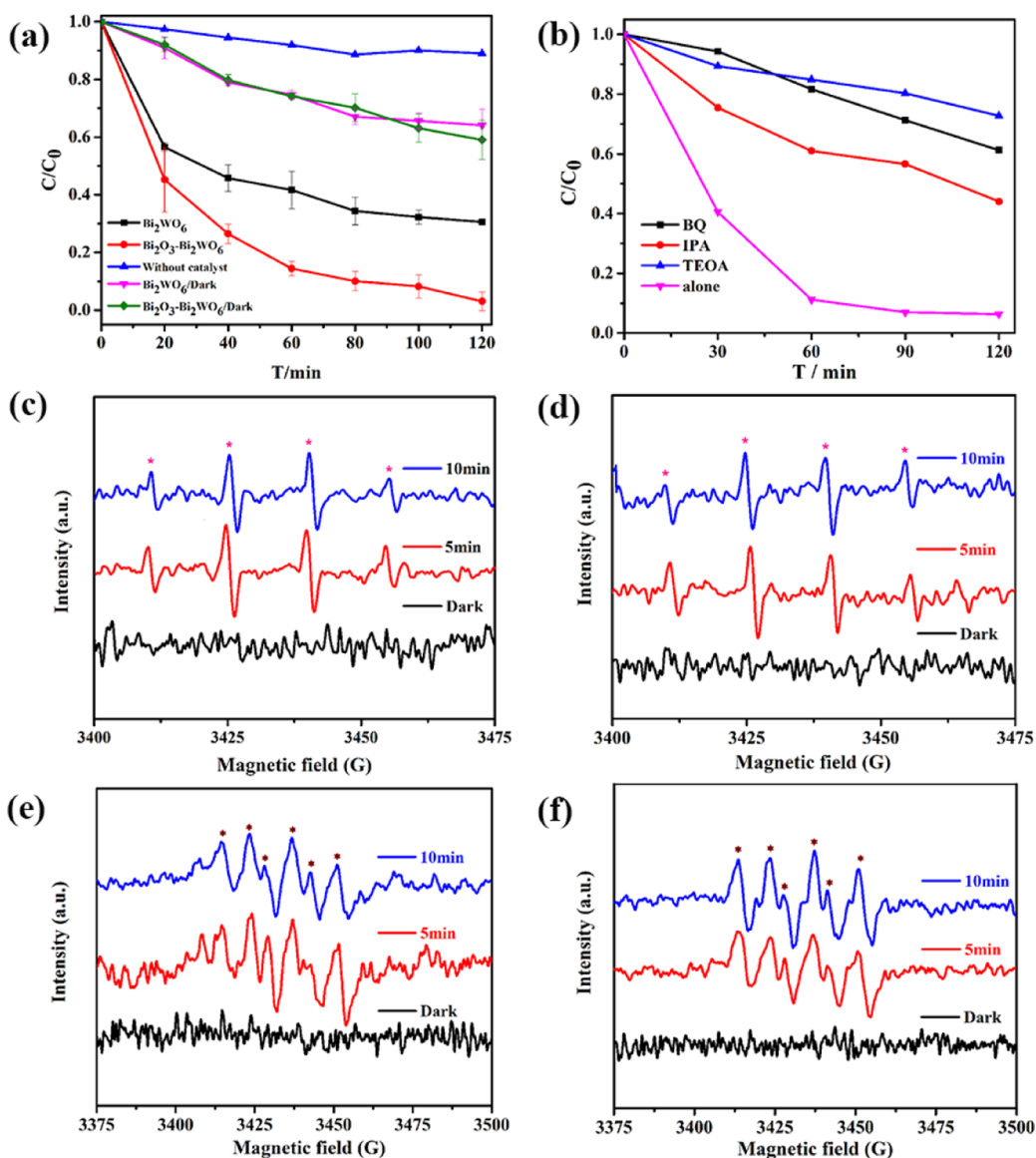


Figure 5. (a) Photodegradation/removal efficiencies of OTC as a function of irradiation time in the presence of Bi_2WO_6 and $\text{Bi}_2\text{O}_3\text{-Bi}_2\text{WO}_6$ composites under visible light irradiation, (b) photocatalytic degradation of OTC over $\text{Bi}_2\text{O}_3\text{-Bi}_2\text{WO}_6$ composites in the presence of different scavengers, (c,e) EPR spectra of DMPO-OH and DMPO- $\text{O}_2^{\bullet-}$ over Bi_2WO_6 under visible light irradiation, and (d,f) EPR spectra of DMPO-OH and DMPO- $\text{O}_2^{\bullet-}$ over $\text{Bi}_2\text{O}_3\text{-Bi}_2\text{WO}_6$ composites under visible light irradiation.

holes (h^+), superoxide radicals ($\text{O}_2^{\bullet-}$), and hydroxyl radicals ($\bullet\text{OH}$) could be trapped by the triethanolamine (TEOA), 1,4-benzoquinone (BQ), and isopropyl alcohol (IPA), respectively.^{26,29,54} As displayed in Figure 5b, the photocatalytic activities of $\text{Bi}_2\text{O}_3\text{-Bi}_2\text{WO}_6$ composites for the degradation of OTC would be restricted to some extent. The photodegradation efficiency of OTC is significantly inhibited upon the addition of TEOA. Similarly, when the BQ and IPA were added to the photocatalytic reaction system, the photodegradation of OTC remarkably reduces. Moreover, the restraining degree of photodegradation of OTC slightly reduces when the IPA is added into the reaction system. In addition, we can clearly see that the trend of photocatalytic degradation of OTC by Bi_2WO_6 influenced by different scavengers (Figure S13) is similar with that of $\text{Bi}_2\text{O}_3\text{-Bi}_2\text{WO}_6$ composites. These results show that the photocatalytic oxidation of OTC over Bi_2WO_6 and $\text{Bi}_2\text{O}_3\text{-Bi}_2\text{WO}_6$ composites under visible light irradiation is driven by the

photogenerated hole–electron pairs, while the activated oxygen is the oxidant driving the degradation of target pollutants.⁵⁵ Besides, the existence of $\bullet\text{OH}$ and $\text{O}_2^{\bullet-}$ radicals generated the photocatalytic process, which was further confirmed using the EPR technique. In the dark, no signal peak of $\bullet\text{OH}$ and $\text{O}_2^{\bullet-}$ radicals was observed (Figure 5c–f). After visible light irradiation, both Bi_2WO_6 and $\text{Bi}_2\text{O}_3\text{-Bi}_2\text{WO}_6$ composites have an obvious EPR signal peak of DMPO- $\bullet\text{OH}$ (the signal intensity ratio is 1:2:2:1) and DMPO- $\text{O}_2^{\bullet-}$ radicals (the signal intensity ratio is 1:1:1:1), which is consistent with the result of trapping experiments.

Based on the abovementioned results, we investigated the mechanism of the enhancement photocatalytic performance of $\text{Bi}_2\text{O}_3\text{-Bi}_2\text{WO}_6$ composites. According to the band structure schematic diagram of Bi_2O_3 reported in the previous literature,⁵⁶ the CB and valence band (VB) edge potentials of Bi_2O_3 and Bi_2WO_6 are displayed in Figure S14a. When p- Bi_2O_3 and n- Bi_2WO_6 formed the heterostructure, the whole

energy band of p-Bi₂O₃ upshifts and that of n-Bi₂WO₆ declines, which would be attributed to the moving of the Fermi level.^{49,57} Under visible light irradiation, Bi₂O₃ would act as an electron-donating semiconductor, making the photoexcited electrons move toward the CB of Bi₂WO₆ (Figure S14b). Meanwhile, the holes in the VB of Bi₂WO₆ would transfer to that of Bi₂O₃ owing to the effect of the inner electric field.⁵⁶ More importantly, the existence of oxygen vacancies would form new defect states below the conduction of Bi₂WO₆.^{58–60} The electrons derived from the CB of Bi₂O₃ would be prone to moving the new electric state vacancy band owing to that the oxygen vacancies could act as charge carrier traps. Therefore, the result would be beneficial to the separation of photo-generated electron–hole pairs, resulting in that the Bi₂O₃–Bi₂WO₆ composites exhibited excellent photocatalytic activity compared with pure Bi₂WO₆.

CONCLUSIONS

In summary, the ultrathin Bi₂O₃–Bi₂WO₆ nanosheet composites have been successfully synthesized via a simple hydrothermal method. Compared to Bi₂WO₆, Bi₂O₃–Bi₂WO₆ composites exhibit excellent photocatalytic activity, which would be the combined effect of the heterojunction structure and the large-sized oxygen defect aroused by the ultrathin structure. The photocatalyst of Bi₂O₃–Bi₂WO₆ composites would possess a great potential to be applied in the environment pollution treatment, especially the aspect of polluted water purification.

ASSOCIATED CONTENT

Supporting Information

The Supporting Information is available free of charge at <https://pubs.acs.org/doi/10.1021/acs.langmuir.1c00576>.

TEM images and EPR spectra of the catalyst, mass spectra of byproducts of OTC and the proposed photodegradation pathway, and photodegradation data of the catalyst (PDF)

AUTHOR INFORMATION

Corresponding Authors

Jinwu Bai – Chongqing Key Laboratory of Catalysis and New Environmental Materials, College of Environment and Resources, Chongqing Technology and Business University, Chongqing 400067, China; Tianjin Key Laboratory of Environmental Remediation and Pollution Control, College of Environment Science and Engineering, Nankai University, Tianjin 300071, China; orcid.org/0000-0002-2178-1817; Email: Baijw@ctbu.edu.cn

Xiaolei Ren – Chongqing Key Laboratory of Catalysis and New Environmental Materials, College of Environment and Resources, Chongqing Technology and Business University, Chongqing 400067, China; Email: xlren@ctbu.edu.cn

Authors

Xue Chen – Tianjin Key Laboratory of Environmental Remediation and Pollution Control, College of Environment Science and Engineering, Nankai University, Tianjin 300071, China

Peng Lu – Chongqing Key Laboratory of Catalysis and New Environmental Materials, College of Environment and Resources, Chongqing Technology and Business University, Chongqing 400067, China

Min Fu – Chongqing Key Laboratory of Catalysis and New Environmental Materials, College of Environment and Resources, Chongqing Technology and Business University, Chongqing 400067, China; orcid.org/0000-0002-3548-053X

Complete contact information is available at:
<https://pubs.acs.org/10.1021/acs.langmuir.1c00576>

Notes

The authors declare no competing financial interest.

ACKNOWLEDGMENTS

This work was supported by the Scientific Research Projects for High-Level Talents of Chongqing Technology and Business University (1956032), youth project of science and technology research program of Chongqing Education Commission of China (no KJQN202000824), the Talent planning project of Chongqing (CQYC201903053), and the Special General Project of Chongqing Technology Innovation and Application Development (no. cstcscx-msxm1374).

REFERENCES

- (1) Novoselov, K. S.; Geim, A. K.; Morozov, S. V.; Jiang, D.; Zhang, Y.; Dubonos, S. V.; Grigorieva, I. V.; Firsov, A. A. Electric field effect in atomically thin carbon films. *Science* **2004**, *306*, 666–669.
- (2) Jo, K.; Gu, M.; Kim, B.-S. Ultrathin supercapacitor electrode based on reduced graphene oxide nanosheets assembled with photo-cross-linkable polymer: conversion of electrochemical kinetics in ultrathin films. *Chem. Mater.* **2015**, *27*, 7982–7989.
- (3) Gao, G.; Wu, H. B.; Dong, B.; Ding, S.; Lou, X. W. D. Growth of ultrathin ZnCo₂O₄ nanosheets on reduced graphene oxide with enhanced lithium storage properties. *Adv. Sci.* **2015**, *2*, 1400014.
- (4) Lu, Z.; Zhu, J.; Sim, D.; Zhou, W.; Shi, W.; Hng, H. H.; Yan, Q. Synthesis of ultrathin silicon nanosheets by using graphene oxide as template. *Chem. Mater.* **2011**, *23*, 5293–5295.
- (5) Liu, Y.; Li, W.; Shen, D.; Wang, C.; Li, X.; Pal, M.; Zhang, R.; Chen, L.; Yao, C.; Wei, Y.; Li, Y.; Zhao, Y.; Zhu, H.; Wang, W.; El-Toni, A. M.; Zhang, F.; Zhao, D. Synthesis of mesoporous silica/reduced graphene oxide sandwich-like sheets with enlarged and “Funneling” mesochannels. *Chem. Mater.* **2015**, *27*, 5577–5586.
- (6) Xie, J.; Zhang, H.; Li, S.; Wang, R.; Sun, X.; Zhou, M.; Zhou, J.; Lou, X. W. D.; Xie, Y. Defect-rich MoS₂ ultrathin nanosheets with additional active edge sites for enhanced electrocatalytic hydrogen evolution. *Adv. Mater.* **2013**, *25*, 5807–5813.
- (7) Yang, Q.; Lu, Z. Y.; Sun, X. M.; Liu, J. F. Ultrathin Co₃O₄ nanosheet arrays with high supercapacitive performance. *Sci. Rep.* **2013**, *3*, 3537.
- (8) Liu, Q.; Wu, D.; Zhou, Y.; Su, H.; Wang, R.; Zhang, C.; Yan, S.; Xiao, M.; Zou, Z. Single-crystalline, ultrathin ZnGa₂O₄ nanosheet scaffolds to promote photocatalytic activity in CO₂ reduction into methane. *ACS Appl. Mater. Interfaces* **2014**, *6*, 2356–2361.
- (9) Hu, C.; Zhang, X.; Li, W.; Yan, Y.; Xi, G.; Yang, H.; Li, J.; Bai, H. Large-scale, ultrathin and (001) facet exposed TiO₂ nanosheet superstructures and their applications in photocatalysis. *J. Mater. Chem. A* **2014**, *2*, 2040–2043.
- (10) Yu, N.; Yin, H.; Zhang, W.; Liu, Y.; Tang, Z.; Zhu, M.-Q. High-performance fiber-shaped all-solid-state asymmetric supercapacitors based on ultrathin MnO₂ nanosheet/carbon fiber cathodes for wearable electronics. *Adv. Energy Mater.* **2016**, *6*, 1501458.
- (11) Gong, Q.; Cheng, L.; Liu, C.; Zhang, M.; Feng, Q.; Ye, H.; Zeng, M.; Xie, L.; Liu, Z.; Li, Y. Ultrathin MoS₂(1-x)Se_{2x} alloy nanoflakes for electrocatalytic hydrogen evolution reaction. *ACS Catal.* **2015**, *5*, 2213–2219.
- (12) Ji, J.; Zhang, L. L.; Ji, H.; Li, Y.; Zhao, X.; Bai, X.; Fan, X.; Zhang, F.; Ruoff, R. S. Nanoporous Ni(OH) thin film on 3D

ultrathin-graphite foam for asymmetric supercapacitor. *ACS Nano* **2013**, *7*, 6237–6243.

(13) He, Y.; Muhetaer, A.; Li, J.; Wang, F.; Liu, C.; Li, Q.; Xu, D. Ultrathin $\text{Li}_4\text{Ti}_5\text{O}_{12}$ nanosheet based hierarchical microspheres for high-rate and long-cycle life li-ion batteries. *Adv. Energy Mater.* **2017**, *7*, 1700950.

(14) Gai, B.; Sun, Y.; Lim, H.; Chen, H.; Faucher, J.; Lee, M. L.; Yoon, J. Multilayer-grown ultrathin nanostructured GaAs solar cells as a cost-competitive materials platform for III-V photovoltaics. *ACS Nano* **2017**, *11*, 992–999.

(15) Lv, M.; Sun, X.; Wei, S.; Shen, C.; Mi, Y.; Xu, X. Ultrathin lanthanum tantalate perovskite nanosheets modified by nitrogen doping for efficient photocatalytic water splitting. *ACS Nano* **2017**, *11*, 11441–11448.

(16) Rangappa, D.; Murukanahally, K. D.; Tomai, T.; Unemoto, A.; Honma, I. Ultrathin nanosheets of Li_2MSiO_4 ($M = \text{Fe}, \text{Mn}$) as high-capacity li-ion battery electrode. *Nano Lett.* **2012**, *12*, 1146–1151.

(17) Guan, M.; Xiao, C.; Zhang, J.; Fan, S.; An, R.; Cheng, Q.; Xie, J.; Zhou, M.; Ye, B.; Xie, Y. Vacancy associates promoting solar-driven photocatalytic activity of ultrathin bismuth oxychloride nanosheets. *J. Am. Chem. Soc.* **2013**, *135*, 10411–10417.

(18) Wu, J.; Guo, P.; Mi, R.; Liu, X.; Zhang, H.; Mei, J.; Liu, H.; Lau, W.-M.; Liu, L.-M. Ultrathin NiCo_2O_4 nanosheets grown on three-dimensional interwoven nitrogen-doped carbon nanotubes as binder-free electrodes for high-performance supercapacitors. *J. Mater. Chem. A* **2015**, *3*, 15331–15338.

(19) Xiong, J.; Wen, L.; Jiang, F.; Liu, Y.; Liang, S.; Wu, L. Ultrathin HNb_3O_8 nanosheet: an efficient photocatalyst for the hydrogen production. *J. Mater. Chem. A* **2015**, *3*, 20627–20632.

(20) Greiner, M. T.; Chai, L.; Helander, M. G.; Tang, W.-M.; Lu, Z.-H. Transition metal oxide work functions: the influence of cation oxidation state and oxygen vacancies. *Adv. Funct. Mater.* **2012**, *22*, 4557–4568.

(21) Wang, G.; Wang, H.; Ling, Y.; Tang, Y.; Yang, X.; Fitzmorris, R. C.; Wang, C.; Zhang, J. Z.; Li, Y. Hydrogen-treated TiO_2 nanowire arrays for photoelectrochemical water splitting. *Nano Lett.* **2011**, *11*, 3026–3033.

(22) Kong, M.; Li, Y.; Chen, X.; Tian, T.; Fang, P.; Zheng, F.; Zhao, X. Tuning the relative concentration ratio of bulk defects to surface defects in TiO_2 nanocrystals leads to high photocatalytic efficiency. *J. Am. Chem. Soc.* **2011**, *133*, 16414–16417.

(23) Mann, A. K. P.; Skrabalak, S. E. Synthesis of single-crystalline nanoplates by spray pyrolysis: a metathesis route to Bi_2WO_6 . *Chem. Mater.* **2011**, *23*, 1017–1022.

(24) Zhang, C.; Zhu, Y. Synthesis of square Bi_2WO_6 nanoplates as high-activity visible-light-driven photocatalysts. *Chem. Mater.* **2005**, *17*, 3537–3545.

(25) Sun, S.; Wang, W.; Zhang, L. Bi_2WO_6 quantum dots decorated reduced graphene oxide: improved charge separation and enhanced photoconversion efficiency. *J. Phys. Chem. C* **2013**, *117*, 9113–9120.

(26) Ding, X.; Zhao, K.; Zhang, L. Enhanced photocatalytic removal of sodium pentachlorophenate with self-doped Bi_2WO_6 under visible light by generating more superoxide ions. *Environ. Sci. Technol.* **2014**, *48*, 5823–5831.

(27) Wang, C.; Zhang, H.; Li, F.; Zhu, L. Degradation and mineralization of bisphenol a by mesoporous Bi_2WO_6 under simulated solar light irradiation. *Environ. Sci. Technol.* **2010**, *44*, 6843–6848.

(28) Chen, M.; Chu, W. Efficient degradation of an antibiotic norfloxacin in aqueous solution via a simulated solar-light-mediated Bi_2WO_6 process. *Ind. Eng. Chem. Res.* **2012**, *51*, 4887–4893.

(29) Huang, H.; Liu, K.; Chen, K.; Zhang, Y.; Zhang, Y.; Wang, S. Ce and F comodification on the crystal structure and enhanced photocatalytic activity of Bi_2WO_6 photocatalyst under visible light irradiation. *J. Phys. Chem. C* **2014**, *118*, 14379–14387.

(30) Tian, N.; Zhang, Y.; Huang, H.; He, Y.; Guo, Y. Influences of Gd substitution on the crystal structure and visible-light-driven photocatalytic performance of Bi_2WO_6 . *J. Phys. Chem. C* **2014**, *118*, 15640–15648.

(31) Zhang, Z.; Wang, W.; Wang, L.; Sun, S. Enhancement of visible-light photocatalysis by coupling with narrow-band-gap semiconductor: a case study on $\text{Bi}_2\text{S}_3/\text{Bi}_2\text{WO}_6$. *ACS Appl. Mater. Interfaces* **2012**, *4*, 593–597.

(32) Shang, M.; Wang, W.; Xu, H. New Bi_2WO_6 nanocages with high visible-light-driven photocatalytic activities prepared in refluxing EG. *Cryst. Growth Des.* **2009**, *9*, 991–996.

(33) Xiao, X.; Wei, J.; Yang, Y.; Xiong, R.; Pan, C.; Shi, J. Photoreactivity and mechanism of g- C_3N_4 and Ag Co-Modified Bi_2WO_6 Microsphere under Visible Light Irradiation. *ACS Sustainable Chem. Eng.* **2016**, *4*, 3017–3023.

(34) Wu, Q.-S.; Feng, Y.; Zhang, G.-Y.; Sun, Y.-Q.; Xu, Y.-Y.; Gao, D.-Z. $\alpha\text{-Fe}_2\text{O}_3$ modified Bi_2WO_6 flower-like mesostructures with enhanced photocatalytic performance. *Mater. Res. Bull.* **2014**, *49*, 440–447.

(35) Zhu, S.; Xu, T.; Fu, H.; Zhao, J.; Zhu, Y. Synergetic effect of Bi_2WO_6 photocatalyst with C-60 and enhanced photoactivity under visible irradiation. *Environ. Sci. Technol.* **2007**, *41*, 6234–6239.

(36) Ren, F.; Zhang, J.; Wang, Y.; Yao, W. A graphene-coupled Bi_2WO_6 nanocomposite with enhanced photocatalytic performance: a first-principles study. *Phys. Chem. Chem. Phys.* **2016**, *18*, 14113–14121.

(37) Wang, H.; Li, S.; Zhang, L.; Chen, Z.; Hu, J.; Zou, R.; Xu, K.; Song, G.; Zhao, H.; Yang, J.; Liu, J. Surface decoration of Bi_2WO_6 superstructures with Bi_2O_3 nanoparticles: an efficient method to improve visible-light-driven photocatalytic activity. *Crystengcomm* **2013**, *15*, 9011–9019.

(38) Li, Z.; Chen, H.-Y. T.; Schouteden, K.; Lauwaet, K.; Janssens, E.; Van Haesendonck, C.; Pacchioni, G.; Lievens, P. Lateral manipulation of atomic vacancies in ultrathin insulating films. *ACS Nano* **2015**, *9*, 5318–5325.

(39) Yang, C.; Gao, G.; Zhang, J.; Liu, R.; Fan, R.; Zhao, M.; Wang, Y.; Gan, S. Surface oxygen vacancy induced solar light activity enhancement of a $\text{CdWO}_4/\text{Bi}_2\text{O}_2\text{CO}_3$ core-shell heterostructure photocatalyst. *Phys. Chem. Chem. Phys.* **2017**, *19*, 14431–14441.

(40) Huang, J.; Tan, G.; Ren, H.; Yang, W.; Xu, C.; Zhao, C.; Xia, A. Photoelectric activity of a $\text{Bi}_2\text{O}_3/\text{Bi}_2\text{WO}_{6-x}\text{F}_{2x}$ heterojunction prepared by a simple one-step microwave hydrothermal method. *ACS Appl. Mater. Interfaces* **2014**, *6*, 21041–21050.

(41) Zhou, L.; Wang, W.; Xu, H.; Sun, S.; Shang, M. Bi_2O_3 hierarchical nanostructures: controllable synthesis, growth mechanism, and their application in photocatalysis. *Chem.—Eur. J.* **2009**, *15*, 1776–1782.

(42) Kong, X. Y.; Choo, Y. Y.; Chai, S.-P.; Soh, A. K.; Mohamed, A. R. Oxygen vacancy induced Bi_2WO_6 for the realization of photocatalytic CO_2 reduction over the full solar spectrum: from the UV to the NIR region. *Chem. Commun.* **2016**, *52*, 14242–14245.

(43) Lv, Y. H.; Yao, W. Q.; Zong, R. L.; Zhu, Y. F. Fabrication of wide-range-visible photocatalyst $\text{Bi}_2\text{WO}_{6-x}$ nanoplates via surface oxygen vacancies. *Sci. Rep.* **2016**, *6*, 19347.

(44) Yan, J.; Wu, G.; Guan, N.; Li, L.; Li, Z.; Cao, X. Understanding the effect of surface/bulk defects on the photocatalytic activity of TiO_2 : anatase versus rutile. *Phys. Chem. Chem. Phys.* **2013**, *15*, 10978–10988.

(45) Shi, W.; Li, Y.; Hou, J.; Lv, H.; Zhao, X.; Fang, P.; Zheng, F.; Wang, S. Densely populated mesopores in microcuboid CeO_2 crystal leading to a significant enhancement of catalytic activity. *J. Mater. Chem. A* **2013**, *1*, 728–734.

(46) Sun, W.; Li, Y.; Shi, W.; Zhao, X.; Fang, P. Formation of AgI/TiO_2 nanocomposite leads to excellent thermo-chromic reversibility and photostability. *J. Mater. Chem.* **2011**, *21*, 9263–9270.

(47) Liu, X.; Zhou, K.; Wang, L.; Wang, B.; Li, Y. Oxygen vacancy clusters promoting reducibility and activity of ceria nanorods. *J. Am. Chem. Soc.* **2009**, *131*, 3140–3141.

(48) Wu, J.; Duan, F.; Zheng, Y.; Xie, Y. Synthesis of Bi_2WO_6 nanoplate-built hierarchical nest-like structures with visible-light-induced photocatalytic activity. *J. Phys. Chem. C* **2007**, *111*, 12866–12871.

(49) Peng, Y.; Yan, M.; Chen, Q.-G.; Fan, C.-M.; Zhou, H.-Y.; Xu, A.-W. Novel onedimensional Bi₂O₃-Bi₂WO₆ p-n hierarchical heterojunction with enhanced photocatalytic activity. *J. Mater. Chem. A* **2014**, *2*, 8517–8524.

(50) Chen, F.; Wu, C.; Wang, J.; François-Xavier, C. P.; Wintgens, T. Highly efficient Z-scheme structured visible-light photocatalyst constructed by selective doping of Ag@AgBr and Co₃O₄ separately on {010} and {110} facets of BiVO₄; pre-separation channel and hole-sink effects. *Appl. Catal., B* **2019**, *250*, 31–41.

(51) Hassandoost, R.; Pouran, S. R.; Khataee, A.; Orooji, Y.; Joo, S. W. Hierarchically structured ternary heterojunctions based on Ce³⁺/Ce⁴⁺ modified Fe₃O₄ nanoparticles anchored onto graphene oxide sheets as magnetic visible-light-active photocatalysts for decontamination of oxytetracycline. *J. Hazard. Mater.* **2019**, *376*, 200–211.

(52) Hu, X.; Li, C.; Song, J.; Zheng, S.; Sun, Z. Multidimensional assembly of oxygen vacancy-rich amorphous TiO₂-BiOBr-sepiolite composite for rapid elimination of formaldehyde and oxytetracycline under visible light. *J. Colloid Interface Sci.* **2020**, *574*, 61–73.

(53) Xu, J.; Bian, Z.; Xin, X.; Chen, A.; Wang, H. Size dependence of nanosheet BiVO₄ with oxygen vacancies and exposed {001} facets on the photodegradation of oxytetracycline. *Chem. Eng. J.* **2018**, *337*, 684–696.

(54) Tian, Y.; Chang, B.; Lu, J.; Fu, J.; Xi, F.; Dong, X. Hydrothermal synthesis of graphitic carbon nitride-Bi₂WO₆ heterojunctions with enhanced visible light photocatalytic activities. *ACS Appl. Mater. Interfaces* **2013**, *5*, 7079–7085.

(55) Zhang, Y.; Xu, Y.-J. Bi₂WO₆: A highly chemoselective visible light photocatalyst toward aerobic oxidation of benzylic alcohols in water. *RSC Adv.* **2014**, *4*, 2904–2910.

(56) Ge, M.; Cao, C.; Li, S.; Zhang, S.; Deng, S.; Huang, J.; Li, Q.; Zhang, K.; Al-Deyab, S. S.; Lai, Y. Enhanced photocatalytic performances of n-TiO₂ nanotubes by uniform creation of p-n heterojunctions with p-Bi₂O₃ quantum dots. *Nanoscale* **2015**, *7*, 11552–11560.

(57) Li, X.; Huang, R.; Hu, Y.; Chen, Y.; Liu, W.; Yuan, R.; Li, Z. A templated method to Bi₂WO₆ hollow microspheres and their conversion to double-shell Bi₂O₃/Bi₂WO₆ hollow microspheres with improved photocatalytic performance. *Inorg. Chem.* **2012**, *51*, 6245–6250.

(58) Xu, L.; Jiang, Q.; Xiao, Z.; Li, X.; Huo, J.; Wang, S.; Dai, L. Plasma-engraved Co₃O₄ nanosheets with oxygen vacancies and high surface area for the oxygen evolution reaction. *Angew. Chem., Int. Ed.* **2016**, *55*, 5277–5281.

(59) Naldoni, A.; Allietta, M.; Santangelo, S.; Marelli, M.; Fabbri, F.; Cappelli, S.; Bianchi, C. L.; Psaro, R.; Dal Santo, V. Effect of nature and location of defects on bandgap narrowing in black TiO₂ nanoparticles. *J. Am. Chem. Soc.* **2012**, *134*, 7600–7603.

(60) Liang, L.; Lei, F.; Gao, S.; Sun, Y.; Jiao, X.; Wu, J.; Qamar, S.; Xie, Y. Single unit cell bismuth tungstate layers realizing robust solar CO₂ reduction to methanol. *Angew. Chem., Int. Ed.* **2015**, *54*, 13971–13974.